Published in final edited form as:
Magn Reson Med. 2013 July ; 70(1): 64–74. doi:10.1002/mrm.24440.

Highly-Accelerated Real-Time Cardiac Cine MRI Using k-t SPARSE-SENSE

Li Feng[1,2,*], **Monvadi B. Srichai**[1], **Ruth P. Lim**[1], **Alexis Harrison**[3], **Wilson King**[4], **Ganesh Adluru**[5], **Edward VR. Dibella**[5], **Daniel K. Sodickson**[1], **Ricardo Otazo**[1], and **Daniel Kim**[5]

[1]The Bernard and Irene Schwartz Center for Biomedical Imaging, Department of Radiology, New York University School of Medicine, New York, NY, 10016

[2]Sackler Institute of Graduate Biomedical Sciences, New York University School of Medicine, New York, NY, 10016

[3]Department of Internal Medicine, University of Utah, Salt Lake City, UT, 84112

[4]Division of Pediatric Cardiology, University of Utah, Salt Lake City, UT, 84112

[5]Department of Radiology, University of Utah, Salt Lake City, UT, 84112

Abstract

For patients with impaired breath-hold capacity and/or arrhythmias, real-time cine MRI may be more clinically useful than breath-hold cine MRI. However, commercially available real-time cine MRI methods using parallel imaging typically yield relatively poor spatio-temporal resolution due to their low image acquisition speed. We sought to achieve relatively high spatial resolution (~2.5mm × 2.5mm) and temporal resolution (~40ms), to produce high-quality real-time cine MR images that could be applied clinically for wall motion assessment and measurement of left ventricular (LV) function. In this work, we present an 8-fold accelerated real-time cardiac cine MRI pulse sequence using a combination of compressed sensing and parallel imaging (k-t SPARSE-SENSE). Compared with reference, breath-hold cine MRI, our 8-fold accelerated real-time cine MRI produced significantly worse qualitative grades (1–5 scale), but its image quality and temporal fidelity scores were above 3.0 (adequate) and artifacts and noise scores were below 3.0 (moderate), suggesting that acceptable diagnostic image quality can be achieved. Additionally, both 8-fold accelerated real-time cine and breath-hold cine MRI yielded comparable LV function measurements, with coefficient of variation < 10% for LV volumes. Our proposed 8-fold accelerated real-time cine MRI with k-t SPARSE-SENSE is a promising modality for rapid imaging of myocardial function.

Keywords

MRI; heart; real-time; cardiac cine; compressed sensing; k-t SPARSE-SENSE

Introduction

Non-invasive assessment of myocardial function plays an important role in the management of various cardiac diseases (1–7). Breath-hold cine MRI with balanced steady-steady free precession (b-SSFP) readout, which is now considered the gold standard for imaging myocardial function, offers good spatial resolution, high blood-to-myocardium contrast, and

Please send correspondence to: Li Feng, MS., Center for Biomedical Imaging, Department of Radiology, New York University School of Medicine, 660 First AVE, New York, NY 10016, Phone: 212-263-3347, Fax: 212-263-7541, Li.Feng@nyumc.org.

exquisite image quality (8,9). However, in patients with impaired breath-hold capacity and/or arrhythmias, breath-hold cine MRI may yield non-diagnostic image quality. In these patients, real-time cine MRI may be more clinically useful than breath-hold cine MRI (10–20).

The spatio-temporal resolution requirements for real-time cine MRI have been described by Setser et al. (18), where the accuracy of left ventricular (LV) function measurements depends on resolution, both spatial and temporal. Commercially available real-time cine MRI methods using dynamic parallel imaging, such as adaptive sensitivity encoding incorporating temporal filtering (TSENSE) (21) or temporal generalized autocalibrating partially parallel acquisitions (TGRAPPA) (22), typically yield relatively low spatio-temporal resolution (12,13), due to their poor image acquisition speed. For example, our clinical real-time cine MRI protocol using TGRAPPA with acceleration factor (R) = 3 produces 2.5 mm × 2.5 mm spatial resolution and 114 ms temporal resolution. For patients with tachycardia (> 100 bpm) or imaging during stress testing, even higher temporal resolution is desirable.

More advanced investigational image processing methods, in conjunction with parallel imaging, have been reported to further accelerate real-time cine MRI. One method utilizes a Karhunen-Loeve transform filter to improve the performance of auto-calibrated TSENSE or TGRAPPA (23). Another method performs motion compensated reconstruction using deformable registration (24). Another recent method performs a retrospective reconstruction to improve spatio-temporal resolution, by performing real-time cine MRI with parallel imaging over multiple cardiac cycles and averaging the results with motion correction techniques (13,14). However, such retrospective reconstruction method may not perform well in patients with arrhythmias, because of its need for averaging results over multiple heart beats.

More advanced investigational image acquisition methods have also been reported to further accelerate real-time cine MRI. The presence of spatial and temporal correlations in cardiac cine datasets can be exploited to further accelerate data acquisition, due to sparsity in the spatial-temporal Fourier domain. One such method is the partially separable function model (25), which has been shown to produce high spatio-temporal resolution for imaging rat hearts (26). Another investigational method is radial k-t SENSE (27), which has been shown to yield 8-fold accelerated real-time cine MR images with 2.3 mm × 2.3 mm spatial resolution and 40 ms temporal resolution. While this state-of-the-art method is very promising, there are challenges associated with non-Cartesian k-space sampling (e.g., gridding, blurring due to k-space trajectory errors).

An alternative image acquisition method to further accelerate real-time cine MRI is compressed sensing (CS) (28), which has been applied to accelerate breath-hold cardiac cine MRI (29–32). These pioneering works have been important developments but have not been applied for real-time cardiac cine MRI. Recently, a new approach called k-t SPARSE-SENSE (33), based on a combination of k-t SPARSE (29) and sensitivity encoding (SENSE) (34), has been applied for first pass cardiac perfusion MRI (33), cardiac T2 mapping (35) and cine phase-contrast MRI (36). Real-time cardiac cine MRI is also a good candidate for k-t SPARSE-SENSE, because the background is static (due to steady state of magnetization) and the dynamic region (e.g., heart) is relatively small. This condition produces a high degree of spatio-temporal correlation, which could be exploited to achieve signal sparsity with an appropriate transform, such as temporal Fourier transform (FFT) (37, 38), temporal principal component analysis (PCA) (30–32) or temporal total variation (temporal TV, a.k.a. temporal gradient operation) (39).

Based on the work by Setser et al (18). and from our clinical experiences, we sought to achieve spatial resolution on the order of 2.5 mm × 2.5 mm and temporal resolution on the order of 40 ms, to produce high-quality real-time cine MR images that could be applied clinically for wall motion assessment and measurement of LV function. In this work, we propose to highly accelerate real-time cine MRI using k-t SPARSE-SENSE. The study evaluates image quality and global function measurements yielded by accelerated real-time cine MRI.

Materials and Methods

k-Space Undersampling: Incoherence and Self-Calibration of Coil Sensitivities

The first major component for high performance in CS is incoherent aliasing artifact due to random k-space undersampling. To achieve a high degree of incoherence in time-series data, a random k-space undersampling pattern with higher density at the center of k-space has been proposed (28–32), with different variable density random k-space undersampling pattern along time, in order to distribute the resulting aliasing artifacts along both k_y, the spatial frequency in the phase-encoding dimension, and t, the temporal dimension. We modified the real-time cine pulse sequence to employ an 8-fold accelerated k_y-t undersampling pattern, as shown in Figure 1a. Note that temporal average of the sampling pattern, k_x-k_y, represents the sampling used to perform self-calibration of coil sensitivities. For more details on the random k-space undersampling pattern, please see references (33,35,36).

Numerical Simulation

The second major component for high performance in CS is sparse representation of the image in a known transform domain. We performed a numerical simulation experiment on fully sampled, breath-held cine MR datasets (one short-axis (SAX) and one long-axis (LAX)) to determine the optimal sparsifying transform and its regularization parameter. The relevant imaging parameters (e.g., spatial resolution, temporal resolution, receiver bandwidth, and flip angle) were similar to the proposed real-time cine MRI protocol (see *Pulse Sequence* section below). The k-t SPARSE-SENSE reconstruction was performed using the steps described in the *Image Reconstruction* section. This subsection describes the methods and results of the preliminary retrospective numerical simulation experiment which was needed for the prospective acceleration strategy.

Primary Sparsifying Transform: Dynamic Region

The regularization weight was determined empirically by comparing between k-t SPARSE-SENSE images and fully sampled cine MR images, as previously described (33,36). Note that k-t SPARSE-SENSE reconstruction was performed on retrospectively 8-fold undersampled data (see Figure 1a for the sampling pattern). Our prior cardiovascular MRI applications of k-t SPARSE-SENSE (33,35,36) reported regularization parameter values ranging from 0.01 to 0.05. Thus, we repeated the experiment with regularization weight ranging from 0.005–0.05 (0.005 steps) and calculated the root-mean-square-error (RMSE) between k-t SPARSE-SENSE and fully-sampled results. Note that, for each sparsifying transform per regularization weight, RMSE was calculated for the cropped view containing mainly the heart. Figure 2c shows the plot of RMSE as a function of regularization parameter for the heart region. Compared with temporal FFT and temporal PCA, temporal TV yielded lower RMSE, and regularization weight = 0.01 yielded the minimal RMSE for temporal TV (see Figure 2a). We also performed visual inspection to confirm high temporal fidelity of myocardial wall motion at 0.01 weight. Given these results, we elected to use temporal TV as our sparsifying transform with regularization weight 0.01.

Secondary Sparsifying Transform: Static Regions

We also performed the same analysis on the static region (e.g., chest wall). Figure 2d shows the plot of RMSE as a function of regularization parameter. Compared with temporal PCA and temporal TV, temporal FFT yielded lower RMSE, suggesting that it is superior for suppression of residual aliasing artifacts arising from the static regions. Therefore, to further suppress residual incoherent aliasing artifacts arising from the background, we elected to add temporal FFT as a secondary orthogonal sparsifying transform. The resultant reconstruction algorithm is a combination of temporal TV and temporal FFT (temporal TV +FFT)), where the regularization weight for temporal FFT was empirically chosen to be ten times lower than that for temporal TV - small enough to not introduce temporal blurring artifacts but large enough to help suppress residual aliasing artifacts arising from the static regions. Given that the regularization weight for temporal FFT is small (0.001), we did not perform a systematic search for the optimum value. Note that both temporal TV and temporal FFT terms were solved simultaneously during reconstruction.

Acceleration Rates

To determine the maximal R with acceptable results, we performed repeated simulation with R ranging from 2–10 (2 steps), where temporal TV with regularization parameter 0.01 and temporal FFT with regularization parameter 0.001 were used for k-t SPARSE-SENSE reconstruction. Figure 3 shows the end-diastolic and end-systolic images for the different R values, as well as their corresponding spatial-temporal plots through the blood-myocardium boundary. These results show that good results can be obtained up to R = 8. Based on this preliminary experiment, we elected to use R =8 for prospective accelerated acquisitions.

Preliminary Evaluation

For completeness, we performed a simulation experiment comparing the performances of temporal FFT, temporal PCA, temporal TV, and temporal TV + FFT, using both fully-sampled SAX and LAX datasets as references. Both temporal FFT and temporal PCA, as shown in Figure 4b,c (x-y plane), produced temporal blurring artifact in the myocardial wall, which are indicated by the white arrows. In contrast, both temporal TV and temporal TV + FFT (Figure 4d,e) did not produce the specific temporal blurring artifact. The signal intensity profiles, through the blood-myocardium boundary, along y-t were also evaluated for all datasets along the white dotted lines drawn on Figure 4a. These spatial-temporal profiles also show more temporal blurring artifacts for the temporal FFT and temporal PCA than temporal TV and temporal TV+FFT. To further evaluate the temporal fidelity, the reconstructed SAX (4 cases) and LAX (4 cases) datasets were randomized for blind evaluation by 4 readers: two cardiologists (A.H., M.B.S.), one pediatric cardiologist (W.K.), and one radiologist (R.P.L.). Each reader independently ranked the temporal fidelity of myocardial wall motion (1–4; highest-lowest). The results, averaged over 4 readers, showed that both temporal TV+FFT (1.9) and temporal TV (2.0) produced better temporal fidelity of myocardial wall motion than temporal FFT (2.9) and temporal PCA (3.0). Compared with temporal TV, temporal TV + FFT yielded 30% lower residual aliasing artifacts in the background (signal-free region outside the body). Based on these preliminary results, we elected to use temporal TV + FFT as the sparsifying transform for accelerated real-time cine MR data reconstruction.

Pulse Sequence

Our proposed 8-fold accelerated, real-time cine MRI sequence was implemented on a whole-body 3T MRI scanner (Tim Trio, Siemens Healthcare, Erlangen, Germany) equipped with a gradient system capable of achieving a maximum gradient strength of 45 mT/m and a slew rate of 200 T/m/s. The radio-frequency excitation was performed using the body coil.

A 6-element body matrix coil array and a spine coil array (with only 6 elements on) were employed for signal reception.

The relevant imaging parameters for real-time cine were: field of view = 300 mm × 300 mm, acquisition matrix size = 128 × 128, spatial resolution = 2.3 mm × 2.3 mm, slice thickness = 8 mm, flip angle = 40°, repetition time/echo time = 2.7/1.37 ms, receiver bandwidth = 1184 Hz/pixel, and temporal resolution = 43.2 ms. The total scan time was 2 heart beats per slice, with 1 heart beat to play dummy pulses to achieve steady state of magnetization, and another heart beat to acquire the cine data.

The relevant imaging parameters for breath-hold cine MRI were: field of view = 300 mm × 300 mm, acquisition image matrix = 192 × 192, spatial resolution = 1.6 mm × 1.6 mm, slice thickness = 8 mm, flip angle = 40°, repetition time / echo time = 37.5/1.2 ms, retrospective electrocardiogram (ECG) gating with 25 reconstructed cardiac phases, receiver bandwidth = 1300 Hz/pixel, and 1.6-fold accelerated GRAPPA reconstruction.

Human Subjects

Twelve healthy human volunteers with no known cardiac disease (11 males and 1 female; mean age = 26.2 ± 2.7 years) and one male patient (age = 45 years) with history of heart transplantation were imaged using both real-time cine and breath-hold cine MRI sequences, to perform pre-clinical testing and confirmation of comparability of global function measurements with breath hold cine MRI. Fifteen consecutive clinical patients (7 males and 8 females; mean age = 49 ± 21 years) were recruited for image quality assessment of real-cine MRI in a clinical setting. Human imaging was performed in accordance with protocols approved by Institutional Review Board and was found to comply with the Health Insurance Portability and Accountability Act (HIPAA). All subjects provided written informed consent.

Experiment I: Image Quality and Global Function Measurement Comparison (real-time vs. breath-hold cine MRI)

In the first experiment, twelve healthy human volunteers were imaged using both pulse sequences in a stack of 12 short-axis planes covering the entire LV, in order to compare their resulting image quality (only three views; base, mid, and apex) and global function measurements including end diastolic volume (EDV), end systolic volume (ESV), stroke volume (SV), and ejection fraction (EF). Real-time cine imaging of the entire LV was performed during free breathing with prospective ECG triggering, and breath-hold cine imaging was performed with 6 separate breath holds (2 slices per breath-hold) with retrospective ECG gating.

Experiment II: Comparison of LV Function by Real-time Cine MRI with prospective ECG triggering vs. Breath-hold Cine MRI with Retrospective ECG gating

In the second experiment, one male patient with history of heart transplantation was imaged to compare global function measurements between two different end-diastolic frames for real-time cine MRI with prospective ECG triggering. We note that in prospective ECG triggering, it may be difficult to capture true end diastole, which may lead to underestimation of EDV, SV and EF when compared with retrospective ECG gated acquisitions. In this patient, we imaged a stack of 14 short-axis planes covering the entire LV, for 2 heart beats, in order to capture true end diastole between the first and second heart beats with prospectively ECG triggered real-time cine MRI. We calculated two sets of global function measurements from this data set: i) first frame defined as end diastole and ii) visually identified end diastolic frame, acquired between the first and second heart beats. For

reference, another stack of 14 short-axis planes was acquired using breath-hold cine MRI with retrospective ECG gating.

Experiment III: Clinical application of real-time Cine MRI

Fifteen patients (7 males and 8 females; mean age = 49 ± 21 years) were recruited to evaluate the performance (e.g., image quality, wall motion, artifacts, noise) of our proposed real-time cine MRI pulse sequence. For patient recruitment, the only inclusion criterion was normal sinus rhythm, and our patient population included different cardiac disease conditions. Given that our study was not aimed at a particular clinical indication, only one cardiac view was acquired per patient (12 patients had SAX, 3 patients had LAX).

Image Reconstruction

k-t SPARSE-SENSE reconstruction was performed off-line in MATLAB (R2011b software; Mathworks, Natick, MA) running on windows Server 2003 Standard 64-bit xp platform (Microsoft Corporation, Redmond, WA). As described in (36), the coil sensitivity maps were self-calibrated by averaging undersampled k-space data over time (see Figure 1b, Figure 6a) and computed using the method described in (40,41). This subsection describes the methods and results of the preliminary experiment to demonstrate that our self-calibrated coil sensitivities are robust. We acquired a data set with external coil calibration data, and compared the results using external coil and self-calibrated coil sensitivities. Figure 5 shows a comparison between self-calibrated and externally acquired (as a pre-scan) coil sensitivities, as well as their resulting k-t SPARSE-SENSE images. Note that the two sets of data are similar. The benefits of self-calibrated coil sensitivities are that they are intrinsically registered with the undersampled data and do not require additional time for acquisition.

For the k-t SPARSE-SENSE reconstruction, the l_1-norm inverse problem (Figure 6b) was solved iteratively using non-linear conjugate gradient algorithm. The overall flowchart of the image reconstruction is illustrated in Figure 6. Reconstruction time per slice was about 4.6 minutes and the total computational time per cine data set (12 slices) was about 1 hour in a computer equipped with an Intel Xeon CPU at 2.27 GHz with 24 GB global memory.

Image Analysis

For each subject, three slices (apex, mid, base) were chosen from both real-time and breath-hold cine sets for image quality assessment. A total of 72 (36 real-time cine; 36 breath-hold cine) datasets were pooled and randomized for blinded qualitative evaluation by four readers described previously. Readers independently scored the image quality (1=non-diagnostic, 2=poor, 3=adequate, 4=good, 5=excellent), temporal fidelity of myocardial wall motion (1=non-diagnostic, 2=poor, 3=adequate, 4=good, 5=excellent), artifact (1=none, 2=mild, 3=moderate, 4=severe, 5=non-diagnostic), and noise level (1=none, 2=mild, 3=moderate, 4=severe, 5=non-diagnostic).

For global function assessment, 24 (12 real-time cine; 12 breath-hold cine) short-axis stacks of cine datasets were pooled and randomized for blinded quantitative evaluation. The same 4 readers independently calculated the EDV, ESV, SV, and EF for each data set.

For comparison of prospective ECG triggered real-time cine MRI and retrospective ECG gated breath-hold cine MRI, one cardiologist (A.H.) analyzed a short-axis stack of real-time cine MRI data with prospective ECG triggering using two different end diastolic frames (1 and 16, where frame 16 was visually defined as true end diastole) and compared their global function measurements with those obtained using a stack of breath-held cine MR data with retrospective ECG gating.

For evaluation of real-time cine MRI in patients, 15 cine datasets were pooled and randomized for blinded evaluation. The same four readers independently scored the image quality, temporal fidelity of myocardial wall motion, artifact, and noise level for each data set.

Statistical Analysis

For image quality comparison, the reported scores, which were averaged over four readers, represent mean ± standard deviation. Statistical analysis was performed using Excel (Microsoft Corporation, Redmond, WA). Wilcoxon signed-rank sum test was used to compare the mean scores between two groups, where $p < 0.05$ was considered to be statistically significant.

For global function comparison, Bland-Altman and coefficient of variation (CV) analyses were performed. In addition, inter-observer variability within each pulse sequence was also assessed by inter-class correlation (ICC).

Results

Experiment I

Figure 7 shows representative sets of real-time cine MR images and breath-hold cine MR images, in five short axis planes from one healthy subject. Both pulse sequences produced good diagnostic overall image quality. Table 1 shows the mean scores of image quality, temporal fidelity of wall motion, artifact, and noise level for breath-hold cine and real-time cine results (n=36). Compared with breath-hold cine, real-time cine yielded significantly ($p < 0.05$) worse scores for all four categories. However, for real-time cine MRI, the image quality and temporal fidelity of wall motion scores were above 3.0 (adequate) and artifacts and noise scores were below 3.0 (moderate), suggesting that acceptable diagnostic image quality can be achieved. According to the Bland-Altman (Figure 8) and CV analyses (Table 2), all four global function measurements, averaged over 4 readers, were in good agreement, with CV less than 10%. The inter-class correlation (Table 3) shows that the inter-observer variability in calculating global function measurements ranged from moderate to strong for real-time cine MRI and moderate to near perfect for breath-hold cine MRI.

Experiment II

Figure 9 shows two potential candidates for an end diastolic frame from the same series of mid-ventricular short-axis images acquired with prospective ECG triggering. In this example, the first candidate is cardiac frame 1, and the second candidate is cardiac frame 16 (denoted as frame N in the Figure). Note that cardiac frame 16 shows larger LV cavity than cardiac frame 1. In the male patient with heart transplantation, defining cardiac frame 1 as end diastole produced EDV = 86ml, ESV = 44ml, SV = 42ml, and EF = 49%. Defining cardiac frame 16 as end diastole produced EDV = 94ml, ESV = 44ml, SV = 49ml, and EF = 53%. The reference breath-held cine MRI with retrospective ECG gating yielded EDV = 99ml, ESV = 44ml, SV = 55ml, and EF = 56%. This comparison shows that our proposed prospective ECG triggered approach of acquiring real-time cine MR data through 2 heart beats will ensure capture of true end diastole.

Experiment III

Figure 10 shows representative real-time cine MR images in two different patients in different cardiac imaging planes. Real-time cine MRI with k-t SPARSE-SENSE consistently yielded high-quality images in all patients. The mean scores of image quality, temporal fidelity, artifact, and noise were 3.7 ± 0.6, 4.3 ± 0.7, 1.7 ± 0.7, and 1.7 ± 0.7, which are similar to the corresponding scores from volunteer data (see Table 1). Again, the image

quality and temporal fidelity of wall motion scores were above 3.0 (adequate) and artifact and noise scores were below 3.0 (moderate).

Discussion

This work demonstrates the feasibility of performing 8-fold accelerated real-time cine MRI using k-t SPARSE-SENSE, by exploiting a high degree of spatiotemporal correlation in cardiac cine MRI data. Our 8-fold accelerated real-time cine MRI protocol can achieve adequate spatial resolution of 2.3 mm × 2.3 mm and relatively high temporal resolution of 43.2 ms, with diagnostically acceptable image quality, high temporal fidelity, and relatively accurate global function measurements. This work also demonstrates an approach to capture end diastole with prospective ECG triggering, by continuously performing real-time cine MRI through the second heart beat and visually identifying end diastolic frame.

While real-time cine MRI yielded significantly worse image quality, temporal fidelity, artifact, and noise scores compared with breath-hold cine MRI, image quality and temporal fidelity scores were above 3.0 (adequate), and artifact and noise scores were below 3.0 (moderate). This trend was also true in 15 patients examined. We note that temporal fidelity scores were above 4.0 (good) in both healthy subjects and patients. Temporal fidelity of myocardial wall motion is particularly important to assess regional wall motion abnormalities in the context of coronary artery diseases.

Previously reported k-t acceleration methods such as k-t GRAPPA (42), k-t SENSE (27,43,44), and PEAK-GRAPPA (44) also exploit spatio-temporal correlations in the time series data in combination with coil sensitivity information. However, sparsity and coil sensitivity encoding are exploited in a different way than in k-t SPARSE-SENSE. These k-t acceleration methods take advantage of sparsity to reduce signal overlap in the sparse domain due to regularly undersampled data and perform a linear reconstruction to unfold the sparse representation using prior information on this sparse representation and coil sensitivity information. These linear algorithms are computationally less demanding. Acceleration is achieved at the expense of signal-to-noise ratio and residual coherent aliasing artifacts, and additional training data are needed to learn the sparse representation. In contrast, in k-t SPARSE-SENSE, the specific sparse representation is not needed and a non-linear reconstruction is used to recover the sparse signal coefficients contaminated by incoherent aliasing artifacts produced by an irregular (pseudo-random) undersampling pattern. This non-linear reconstruction is computationally more demanding. Acceleration is achieved at the expense of residual incoherent aliasing artifacts and loss of low signal coefficients in the sparse domain, and it does not require training data.

The proposed 8-fold accelerated real-time cine pulse sequence is a promising investigational method for rapid imaging of myocardial function, particularly for patients with impaired breath-hold capacity, arrhythmias and/or tachycardia. While this new pulse sequence may be clinically useful, we describe several issues that warrant discussion below.

First, in our preliminary work (37,38), only temporal FFT was adopted as the sparsifying transform, which produced temporal blurring of myocardial wall motion. In this work, a combination of temporal TV and temporal FFT was utilized to sparsify the data (Figure 4e), where the regularization weight for temporal TV was empirically set to be ten times larger than that for the temporal FFT. We note that the use of temporal FFT as a secondary sparsifying transform with a low regularization weight reduces residual incoherent aliasing artifacts. Temporal FFT and temporal PCA are good sparsifying transforms to reduce aliasing artifacts because artifacts are spread incoherently over the entire y-f space and y-pca space, respectively. They also exploit the correlation and redundancy over the whole

dynamic series. However, some signal coefficients with small signal intensity are also suppressed along with incoherent aliasing artifacts, and this leads to temporal blurring artifacts (37,38), as shown in Figure 4b,c. Temporal TV, on the other hand, exploits temporal correlation by taking the gradient of two adjacent temporal frames, producing less temporal blurring than temporal FFT and temporal PCA, as shown in Figure 4d,e.

Second, we observed that regularization parameters in k-t SPARSE-SENSE are crucial. For example, larger parameters produce less residual artifacts at the expense of temporal blurring, and vice versa. In the current implementation, we did not apply any rigorous mathematical criteria to systematically select the regularization parameter. Instead, they were determined empirically based on numerical analysis (see *Numerical Simulation*). This empirical approach is based on our prior CS work in cardiovascular MRI applications (33,35,36), where a fully sampled dataset was retrospectively undersampled and reconstructed to “fine tune” the regularization parameter. Mathematical tools, such as the L-curve, might be a systematic approach to derive regularization parameters. Another approach is to reformulate the CS reconstruction with a regularization parameter based on noise

$$\min \left\| T \bullet d \right\|_1, \text{subject to} \left\| F \bullet d - m \right\|_2^2 \le \varepsilon$$

, where T is the sparsifying transform, F is the Fourier transform operator, d is the image series to be reconstructed, m is the k-space measurement, and ε is the noise variance (k-space Gaussian noise). This formulation converges to the same solution, depending on the choice of **ε,** as the lagrangian form used here, as previously described in (45). Another approach is to implement parameter-free CS reconstruction, where noise is used to derive the regularization parameter (46). While these approaches may offer an easier more physically-based way to tune regularization parameters, it may require an additional acquisition for noise estimation. In this study, our focus was to produce high-quality cardiac images, rather than to develop a method to produce optimum results accounting for the entire field of view. Therefore, we elected to determine empirically the regularization weight based on numerical simulation to evaluate the fidelity of cardiac structures and wall motion.

Third, compared with breath-hold cine MRI using retrospective ECG gating, our accelerated real-time cine MRI with prospective ECG triggering with cardiac frame 1 defined as end diastole underestimated EDV, SV, and EF, because of the finite time needed to detect the ECG trigger and acquire an image. We have proposed an alternative approach to overcome this limitation in the future studies, by acquiring real-time cine data with prospective ECG triggering for 2 heart beats and visually identifying a frame that best represents end diastole (Figure 9).

Fourth, we used the proposed k-space sampling pattern (see Figure 1a) based on our prior experience (33,35,36). Other k-space undersampling patterns were not evaluated. Fifth, our study was carried out in a small number of healthy volunteers and patients with cardiac disease and no arrhythmias. Further studies in a larger cohort of patients with a variety of heart disease encountered in clinical practice are necessary to fully evaluate the clinical utility of the proposed accelerated real-time cine MRI. Sixth, we performed real-time cine MRI during free breathing. As such, our LV function measurements may be contaminated with respiratory motion. We note that this is an issue for all other real-time cine MRI methods performed during free breathing. One solution to minimize this problem is to perform imaging with breath holding. Another solution is to perform imaging with respiratory bellows gating, which is compatible for maintaining steady state of

magnetization for b-SSFP imaging. Lastly, the current implementation of k-t SPARSE-SENSE performs the reconstruction of each slice series serially. Parallel computing could be used to reduce the reconstruction time.

Conclusions

In conclusion, 8-fold real-time cine MRI with k-t SPARSE-SENSE can be used to achieve adequate spatial resolution (2.3 mm × 2.3 mm) and relatively high temporal resolution (43 ms), with good image quality and relatively accurate global function measurements. This 8-fold accelerated real-time cine MRI pulse sequence may be useful for patients with reduced breath-hold capacity, arrhythmia, and/or tachycardia for qualitative assessment of wall motion and quantitative assessment of LV function.

Acknowledgments

The authors would like to acknowledge the following grant support:

National Institutes of Health: R01-EB000447-07A1

American Heart Association: 0730143N

This project was also supported by grant number K12HS019473 from the Agency for Healthcare Research and Quality. The content is solely the responsibility of the authors and does not necessarily represent the official views of the Agency for Healthcare Research and Quality.

References

1. Atkinson DJ, Edelman RR. Cineangiography of the heart in a single breath hold with a segmented turboFLASH sequence. Radiology. 1991; 178(2):357–360. [PubMed: 1987592]
2. Sakuma H, Fujita N, Foo TK, Caputo GR, Nelson SJ, Hartiala J, Shimakawa A, Higgins CB. Evaluation of left ventricular volume and mass with breath-hold cine MR imaging. Radiology. 1993; 188(2):377–380. [PubMed: 8327681]
3. Schulen V, Schick F, Loichat J, Helber U, Huppert PE, Laub G, Claussen CD. Evaluation of K-space segmented cine sequences for fast functional cardiac imaging. Invest Radiol. 1996; 31(8): 512–522. [PubMed: 8854198]
4. Epstein FH, Wolff SD, Arai AE. Segmented k-space fast cardiac imaging using an echo-train readout. Magn Reson Med. 1999; 41(3):609–613. [PubMed: 10204886]
5. Bellenger NG, Grothues F, Smith GC, Pennell DJ. Quantification of right and left ventricular function by cardiovascular magnetic resonance. Herz. 2000; 25(4):392–399. [PubMed: 10948775]
6. White HD, Norris RM, Brown MA, Brandt PW, Whitlock RM, Wild CJ. Left ventricular end-systolic volume as the major determinant of survival after recovery from myocardial infarction. Circulation. 1987; 76(1):44–51. [PubMed: 3594774]
7. Levy D, Garrison RJ, Savage DD, Kannel WB, Castelli WP. Prognostic implications of echocardiographically determined left ventricular mass in the Framingham Heart Study. N Engl J Med. 1990; 322(22):1561–1566. [PubMed: 2139921]
8. Barkhausen J, Goyen M, Ruhm SG, Eggebrecht H, Debatin JF, Ladd ME. Assessment of ventricular function with single breath-hold real-time steady-state free precession cine MR imaging. AJR Am J Roentgenol. 2002; 178(3):731–735. [PubMed: 11856708]
9. Carr JC, Simonetti O, Bundy J, Li D, Pereles S, Finn JP. Cine MR angiography of the heart with segmented true fast imaging with steady-state precession. Radiology. 2001; 219(3):828–834. [PubMed: 11376278]
10. Kerr AB, Pauly JM, Hu BS, Li KC, Hardy CJ, Meyer CH, Macovski A, Nishimura DG. Real-time interactive MRI on a conventional scanner. Magn Reson Med. 1997; 38(3):355–367. [PubMed: 9339436]

11. Yang PC, Kerr AB, Liu AC, Liang DH, Hardy C, Meyer CH, Macovski A, Pauly JM, Hu BS. New real-time interactive cardiac magnetic resonance imaging system complements echocardiography. J Am Coll Cardiol. 1998; 32(7):2049–2056. [PubMed: 9857892]
12. Kellman P, Chefd'hotel C, Lorenz CH, Mancini C, Arai AE, McVeigh ER. Fully automatic, retrospective enhancement of real-time acquired cardiac cine MR images using image-based navigators and respiratory motion-corrected averaging. Magn Reson Med. 2008; 59(4):771–778. [PubMed: 18302227]
13. Kellman P, Chefd'hotel C, Lorenz CH, Mancini C, Arai AE, McVeigh ER. High spatial and temporal resolution cardiac cine MRI from retrospective reconstruction of data acquired in real time using motion correction and resorting. Magn Reson Med. 2009; 62(6):1557–1564. [PubMed: 19780155]
14. Hansen MS, Sorensen TS, Arai AE, Kellman P. Retrospective reconstruction of high temporal resolution cine images from real-time MRI using iterative motion correction. Magn Reson Med. 2011 Dec 21. [Epub ahead of print]. 10.1002/mrm.23284
15. Beer M, Stamm H, Machann W, Weng A, Goltz JP, Breunig F, Weidemann F, Hahn D, Kostler H. Free breathing cardiac real-time cine MR without ECG triggering. Int J Cardiol. 2010; 145(2): 380–382. [PubMed: 20223537]
16. Kaji S, Yang PC, Kerr AB, Tang WH, Meyer CH, Macovski A, Pauly JM, Nishimura DG, Hu BS. Rapid evaluation of left ventricular volume and mass without breath-holding using real-time interactive cardiac magnetic resonance imaging system. J Am Coll Cardiol. 2001; 38(2):527–533. [PubMed: 11499748]
17. Nagel E, Schneider U, Schalla S, Ibrahim T, Schnackenburg B, Bornstedt A, Klein C, Lehmkuhl HB, Fleck E. Magnetic resonance real-time imaging for the evaluation of left ventricular function. J Cardiovasc Magn Reson. 2000; 2(1):7–14. [PubMed: 11545110]
18. Setser RM, Fischer SE, Lorenz CH. Quantification of left ventricular function with magnetic resonance images acquired in real time. J Magn Reson Imaging. 2000; 12(3):430–438. [PubMed: 10992310]
19. Plein S, Smith WH, Ridgway JP, Kassner A, Beacock DJ, Bloomer TN, Sivananthan MU. Qualitative and quantitative analysis of regional left ventricular wall dynamics using real-time magnetic resonance imaging: comparison with conventional breath-hold gradient echo acquisition in volunteers and patients. J Magn Reson Imaging. 2001; 14(1):23–30. [PubMed: 11436210]
20. Hori Y, Yamada N, Higashi M, Hirai N, Nakatani S. Rapid evaluation of right and left ventricular function and mass using real-time true-FISP cine MR imaging without breath-hold: comparison with segmented true-FISP cine MR imaging with breath-hold. J Cardiovasc Magn Reson. 2003; 5(3):439–450. [PubMed: 12882075]
21. Kellman P, Epstein FH, McVeigh ER. Adaptive sensitivity encoding incorporating temporal filtering (TSENSE). Magn Reson Med. 2001; 45(5):846–852. [PubMed: 11323811]
22. Breuer FA, Kellman P, Griswold MA, Jakob PM. Dynamic autocalibrated parallel imaging using temporal GRAPPA (TGRAPPA). Magn Reson Med. 2005; 53(4):981–985. [PubMed: 15799044]
23. Ding Y, Chung YC, Jekic M, Simonetti OP. A new approach to autocalibrated dynamic parallel imaging based on the Karhunen-Loeve transform: KL-TSENSE and KL-TGRAPPA. Magn Reson Med. 2011; 65(6):1786–1792. [PubMed: 21254210]
24. Xue H, Ding Y, Guetter C, Jolly MP, Guehring J, Zuehlsdorff S, Simonetti OP. Motion compensated magnetic resonance reconstruction using inverse-consistent deformable registration: application to real-time cine imaging. Med Image Comput Comput Assist Interv. 2011; 14(Pt 1): 564–572. [PubMed: 22003663]
25. Liang Z-P. Spatiotemporal imaging with partially separable functions. IEEE, ISBI 2007. 2007:988–991.
26. Brinegar, C.; Wu, YJ.; Foley, LM.; Hitchens, T.; Ye, Q.; Ho, C.; ZPL. Real-time cardiac MRI without triggering, gating, or breath holding. Conf Proc IEEE Eng Med Biol Soc; 2008. p. 3381-3384.
27. Muthurangu V, Lurz P, Critchely JD, Deanfield JE, Taylor AM, Hansen MS. Real-time assessment of right and left ventricular volumes and function in patients with congenital heart disease by using

high spatiotemporal resolution radial k-t SENSE. Radiology. 2008; 248(3):782–791. [PubMed: 18632528]

28. Lustig M, Donoho D, Pauly JM. Sparse MRI: The application of compressed sensing for rapid MR imaging. Magn Reson Med. 2007; 58(6):1182–1195. [PubMed: 17969013]
29. Lustig, M.; Santos, J.; Donoho, D.; Pauly, J. k-t SPARSE: high frame rate dynamic MRI exploiting spatio-temporal sparsity. Proceedings of the 14th Annual Meeting of ISMRM; Seattle. 2006. p. 2420
30. Jung H, Park J, Yoo J, Ye JC. Radial k-t FOCUSS for high-resolution cardiac cine MRI. Magn Reson Med. 2010; 63(1):68–78. [PubMed: 19859952]
31. Jung H, Sung K, Nayak KS, Kim EY, Ye JC. k-t FOCUSS: a general compressed sensing framework for high resolution dynamic MRI. Magn Reson Med. 2009; 61(1):103–116. [PubMed: 19097216]
32. Jung H, Ye JC, Kim EY. Improved k-t BLAST and k-t SENSE using FOCUSS. Phys Med Biol. 2007; 52(11):3201–3226. [PubMed: 17505098]
33. Otazo R, Kim D, Axel L, Sodickson DK. Combination of compressed sensing and parallel imaging for highly accelerated first-pass cardiac perfusion MRI. Magn Reson Med. 2010; 64(3):767–776. [PubMed: 20535813]
34. Pruessmann KP, Weiger M, Scheidegger MB, Boesiger P. SENSE: sensitivity encoding for fast MRI. Magn Reson Med. 1999; 42(5):952–962. [PubMed: 10542355]
35. Feng L, Otazo R, Jung H, Jensen JH, Ye JC, Sodickson DK, Kim D. Accelerated cardiac T2 mapping using breath-hold multiecho fast spin-echo pulse sequence with k-t FOCUSS. Magn Reson Med. 2011; 65(6):1661–1669. [PubMed: 21360737]
36. Kim D, Dyvorne HA, Otazo R, Feng L, Sodickson DK, Lee VS. Accelerated phase-contrast cine MRI using k-t SPARSE-SENSE. Magn Reson Med. 2012; 67(4):1054–1064. [PubMed: 22083998]
37. Feng, L.; Otazo, R.; Srichai, M.; Lim, P.; Sodickson, DK.; Kim, D. Highly- Accelerated Real-Time Cine MRI Using Compressed Sensing and Parallel Imaging. Proceedings of the 14th Annual Meeting of ISMRM; Stockholm. 2010. p. 3602
38. Feng, L.; Otazo, R.; Srichai, M.; Lim, P.; Sodickson, DK.; Kim, D. Highly- Accelerated Real-Time Cine MRI using Compressed Sensing and Parallel Imaging with Cardiac Motion Constrained Reconstruction. Proceedings of the 14th Annual Meeting of ISMRM; Montreal. 2011. p. 748
39. Adluru G, Dibella EV. Reordering for improved constrained reconstruction from undersampled k-space data. Int J Biomed Imaging. 2008; 2008:341684. [PubMed: 19096715]
40. Walsh DO, Gmitro AF, Marcellin MW. Adaptive reconstruction of phased array MR imagery. Magn Reson Med. 2000; 43(5):682–690. [PubMed: 10800033]
41. Griswold, MAWD.; Heidemann, RM.; Haase, A.; Jakob, PM. The use of an adaptive reconstruction for array coil sensitivity mapping and intensity normalization. Proceedings of the 10th Annual Meeting of ISMRM; Honolulu, Hawaii, USA. 2002. p. 2410
42. Huang F, Akao J, Vijayakumar S, Duensing GR, Limkeman M. k-t GRAPPA: a k-space implementation for dynamic MRI with high reduction factor. Magn Reson Med. 2005; 54(5): 1172–1184. [PubMed: 16193468]
43. Baltes C, Kozerke S, Hansen MS, Pruessmann KP, Tsao J, Boesiger P. Accelerating cine phase-contrast flow measurements using k-t BLAST and k-t SENSE. Magn Reson Med. 2005; 54(6): 1430–1438. [PubMed: 16276492]
44. Jung B, Ullmann P, Honal M, Bauer S, Hennig J, Markl M. Parallel MRI with extended and averaged GRAPPA kernels (PEAK-GRAPPA): optimized spatiotemporal dynamic imaging. J Magn Reson Imaging. 2008; 28(5):1226–1232. [PubMed: 18972331]
45. Becker S, Bobin J, Candès EJ. NESTA: a fast and accurate first-order method for sparse recovery. SIAM J on Imaging Sciences. 2009; 4(1):1–39.
46. Doneva, M.; Nielsen, T.; Börnert, P. Parameter-Free Compressed Sensing Reconstruction using Statistical Non-Local Self-Similarity Filtering. Proceedings of the 20th Annual Meeting of ISMRM; Melbourne. 2012. p. 74

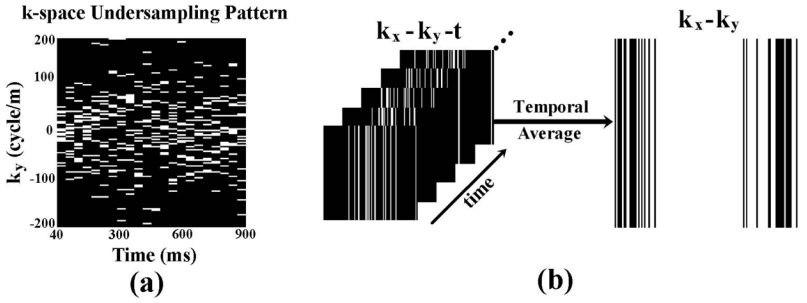

Figure 1.

a) 8-fold accelerated k_y-t sampling pattern varied along time. **b)** A schematic illustrating how the k_x-k_y-t sampling pattern is averaged over time to produce the resulting k_x-k_y sampling pattern. This k_x-k_y pattern represents the sampling used to perform self-calibration of coil sensitivities (see Figure 6 for cross-reference). White lines represent acquired samples.

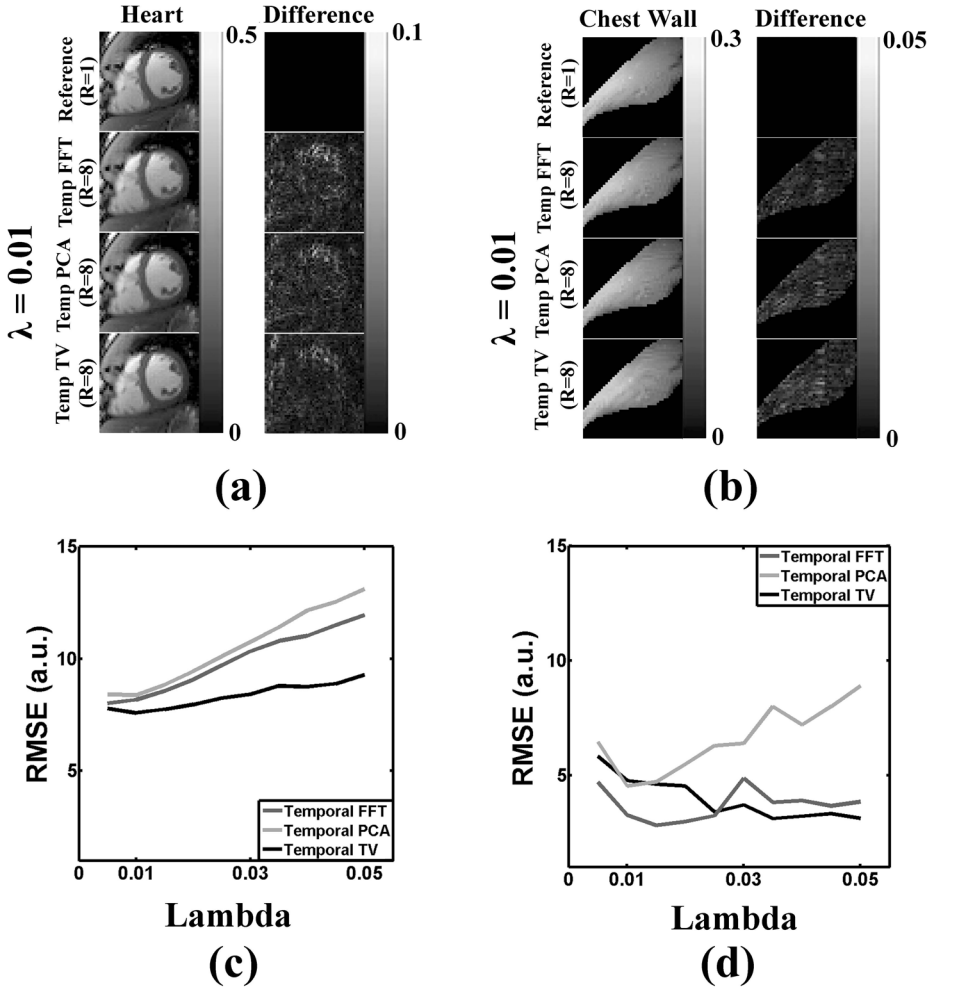

Figure 2.

Simulation results comparing the fully sampled reference cardiac cine data to retrospectively 8-fold accelerated k-t SPARSE-SENSE results with different sparsifying transforms with regularization weight 0.01: temporal FFT, temporal PCA, and temporal TV. a) In the zoomed view of the heart, temporal TV yielded the lowest RMSE. b) In the chest wall, temporal FFT yielded the lowest RMSE. c,d) Corresponding plots of RMSE for the heart and chest wall regions, respectively, as a function of regularization weight ranging from 0.005 to 0.05. These results show that temporal TV is superior to the other two sparsifying transforms for the dynamic region, whereas temporal FFT is superior to the other two transforms for the static region. Based on these results, we elected to use temporal TV as the primary sparsifying transform with regularization weight 0.01 and temporal FFT as the secondary transform with regularization weight 0.001.

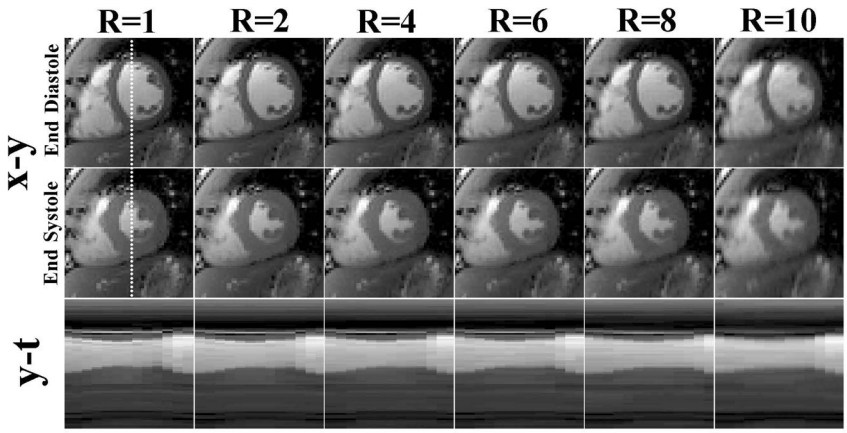

Figure 3.

Numerical simulation results (top row: end-diastolic images, middle row: end-systolic images, bottom row: spatial-temporal plots through the blood-myocardium boundary) comparing different R values using temporal TV with weight 0.01 and temporal FFT with weight 0.001: (first column) R = 1, (second column) R = 2, (third column) R =4, (fourth column) R = 6, (fifth column) R=8, and (sixth column) R = 10. These results show good results can be obtained up to R = 8.

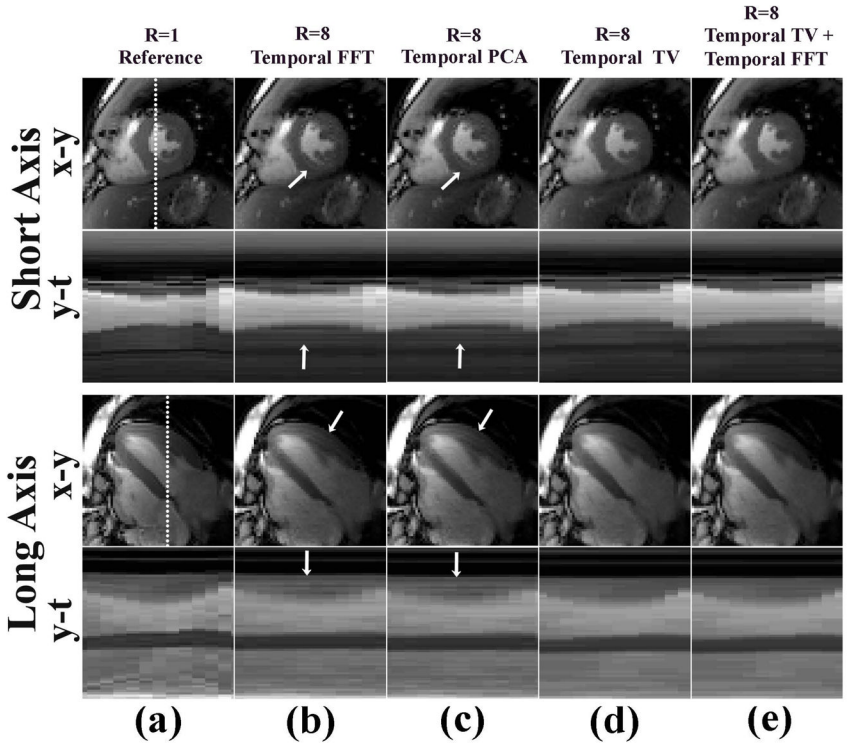

Figure 4.

Numerical simulation results comparing the a) fully-sampled data (R=1) to the retrospectively 8-fold undersampled reconstruction results using four different sparsifying transforms: **b)** temporal FFT, **c)** temporal PCA, **d)** temporal TV, and **e)** temporal TV + FFT. (First row) end-systolic SAX image, (second row) spatial-temporal profile from the SAX image, (third row) end-systolic LAX image, and (fourth row) spatial-temporal profile from the LAX image. Both temporal FFT and temporal PCA yielded more temporal blurring artifacts within the wall (arrows) than temporal TV and temporal TV+FFT.

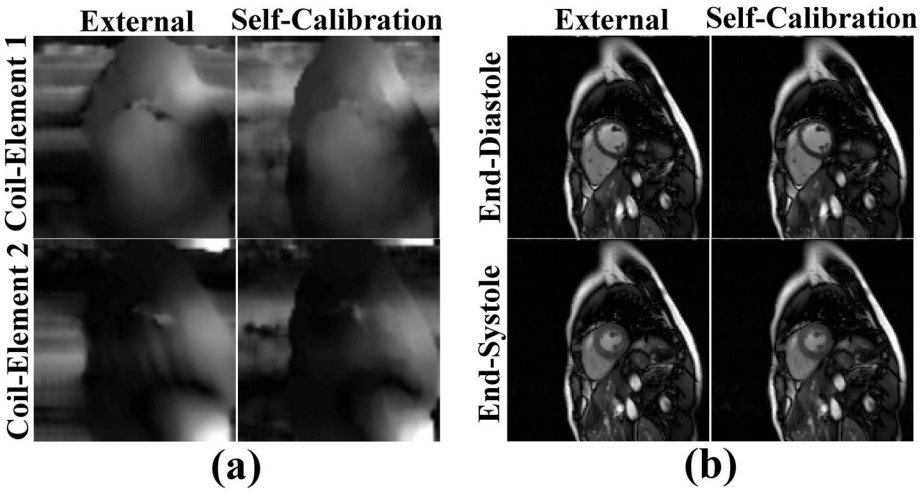

Figure 5.

a) Coil sensitivities calculated using an (left column) external reference acquisition (pre-scan) and (right column) self-calibration method. **b)** The resulting k-t SPARSE-SENSE images using externally and self-calibrated coil sensitivities. Note that two sets of data are very similar, suggesting that our self-calibration of coil sensitivities was robust.

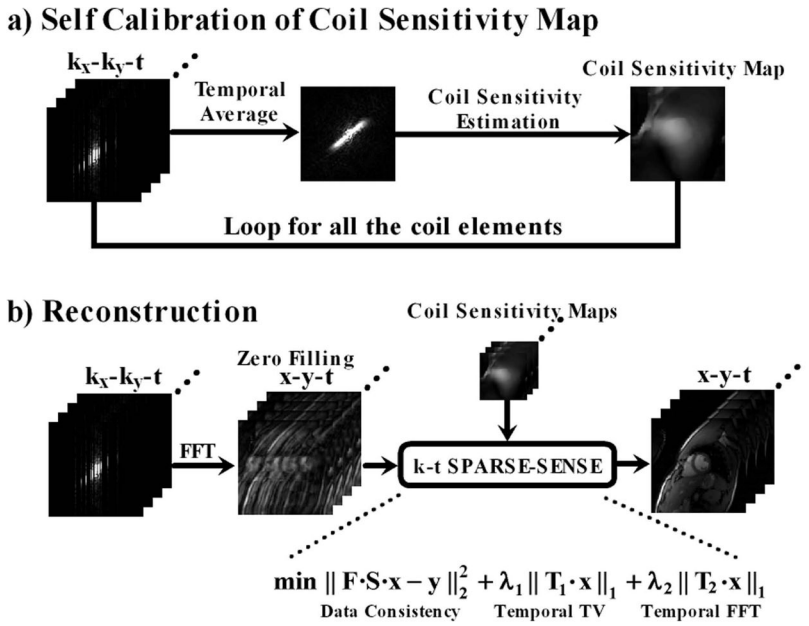

Figure 6.

Schematic flowchart of the image reconstruction method. **a)** Coil sensitivity maps were self-calibrated by averaging undersampled k-space data over time and computed using the adaptive array combination method. **b)** Multicoil, zero-filled k-space data, along with the corresponding coil sensitivity maps, were reconstructed using both temporal TV and temporal FFT as the sparsifying transforms, where regularization weight of temporal TV (λ_1) is ten times larger than that for temporal FFT (λ_2). F: 2D spatial FFT; S: coil sensitivity data; T_1: temporal TV; T_2: temporal FFT; x: image to be reconstructed; y: acquired undersampled k-space; λ_1 and λ_2: regularization parameters.

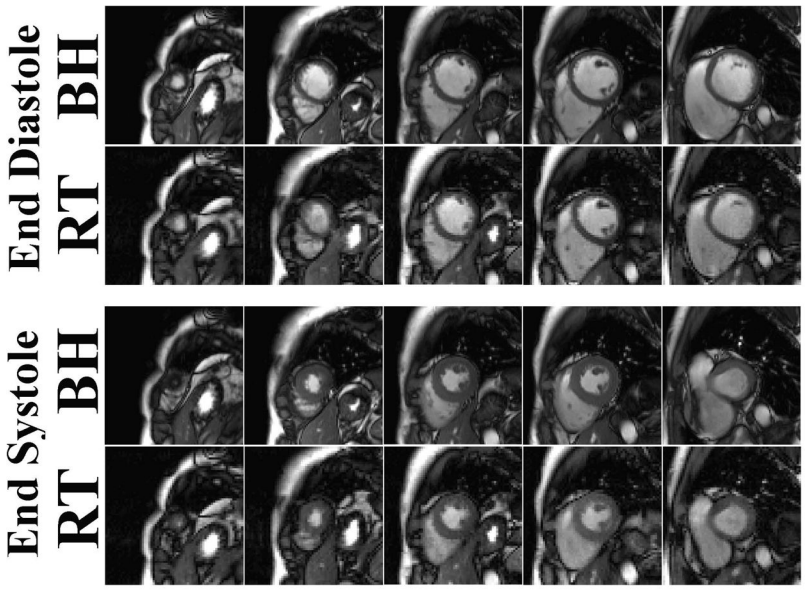

Figure 7.

(Rows 1–2) End-diastolic and (rows 3–4) end-systolic images at multiple cardiac phases comparing (row 1, 3) breath-hold cine MRI and (row 2, 4) real-time cine MRI. Both image sets were acquired from a 29-year old (male) healthy subject. The real-time cine MRI produced averaged scores of 3.25, 4.3, 2.6, and 2.4 for image quality, temporal fidelity, artifact and noise level, respectively, whereas the corresponding scores for breath-hold cine MRI were 4.9, 5, 1.1, and 1.1, respectively. RT: real-time; BH: breath-hold. Note that the breath-hold cine MR images had higher spatial resolution than the real-time cine MR images (1.6 mm vs. 2.3 mm, respectively).

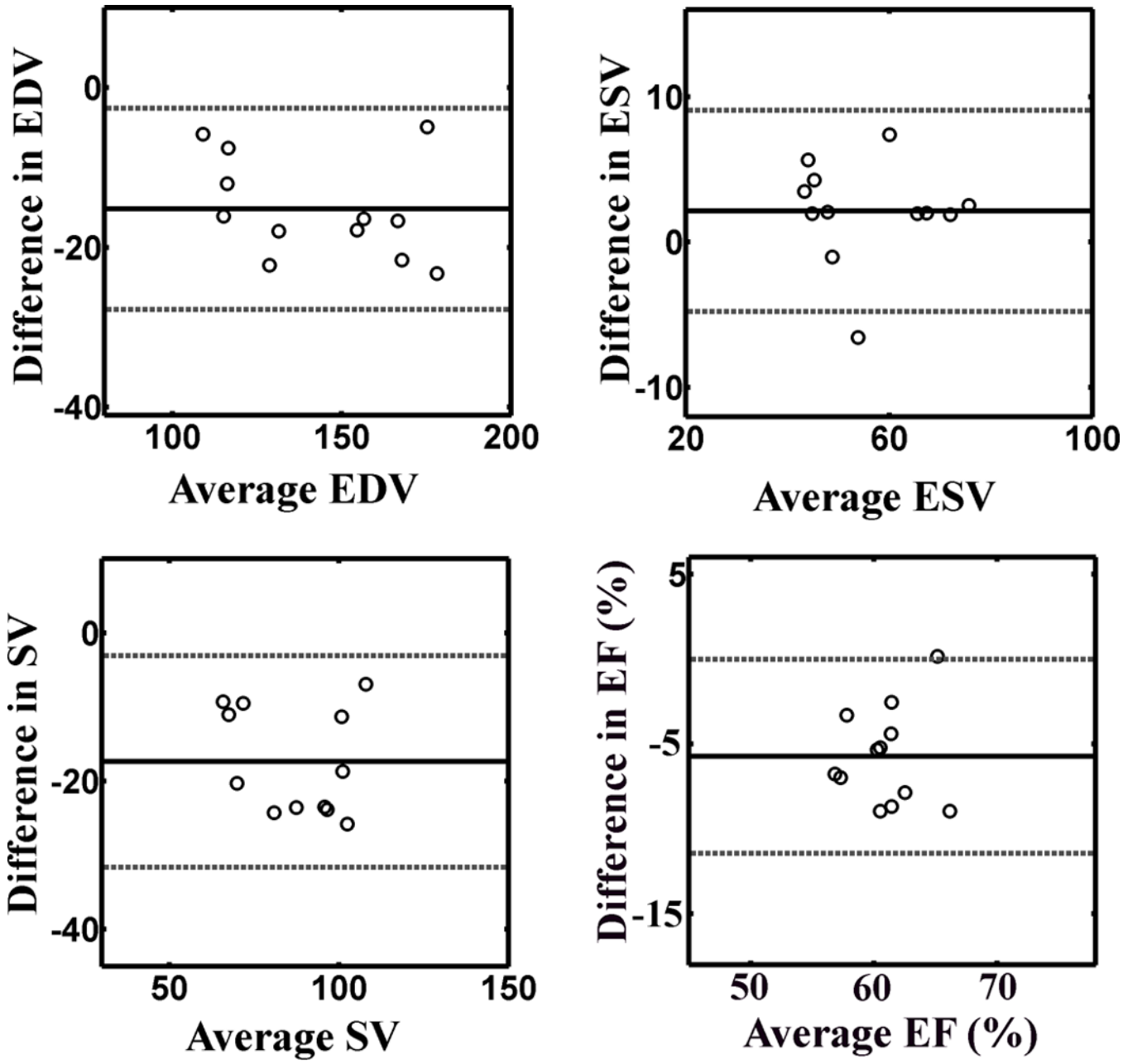

Figure 8.

Bland-Altman plots illustrating good agreement between breath-hold cine MRI and real-time cine MRI for the following LV function measurements: (top, left) EDV (mean difference −15.2 ml [solid line]; lower and upper 95% limits of agreement −27.6 and −2.8 ml [dashed lines], respectively), (top, right) ESV (mean difference 2.1 ml [solid line]; lower and upper 95% limits of agreement −4.7 and 8.9 ml [dashed lines], respectively), (bottom, left) SV (mean difference −17.3 ml [solid line]; lower and upper 95% limits of agreement −31.3 and −3.3 ml [dashed lines], respectively), and (bottom, right) EF (mean difference −5.7 % [solid line]; lower and upper 95% limits of agreement −11.3 % and −0.1 % [dashed lines], respectively).

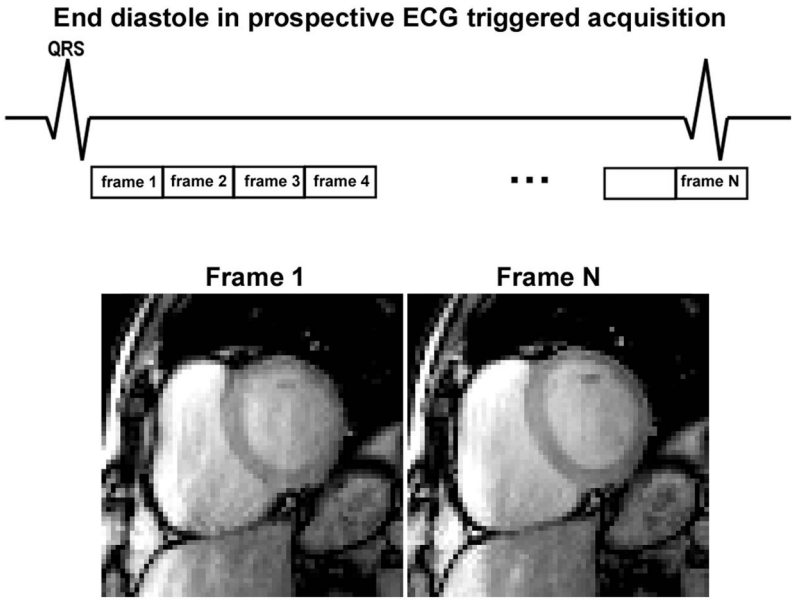

Figure 9.
Proposed real-time cine MRI protocol with prospective ECG triggering to capture true end diastole, where images are continuously acquired through the second R-wave to visually identify true end diastole. This proposed approach yielded global function measurements in excellent agreement with breath-hold cine MRI with retrospective ECG gating.

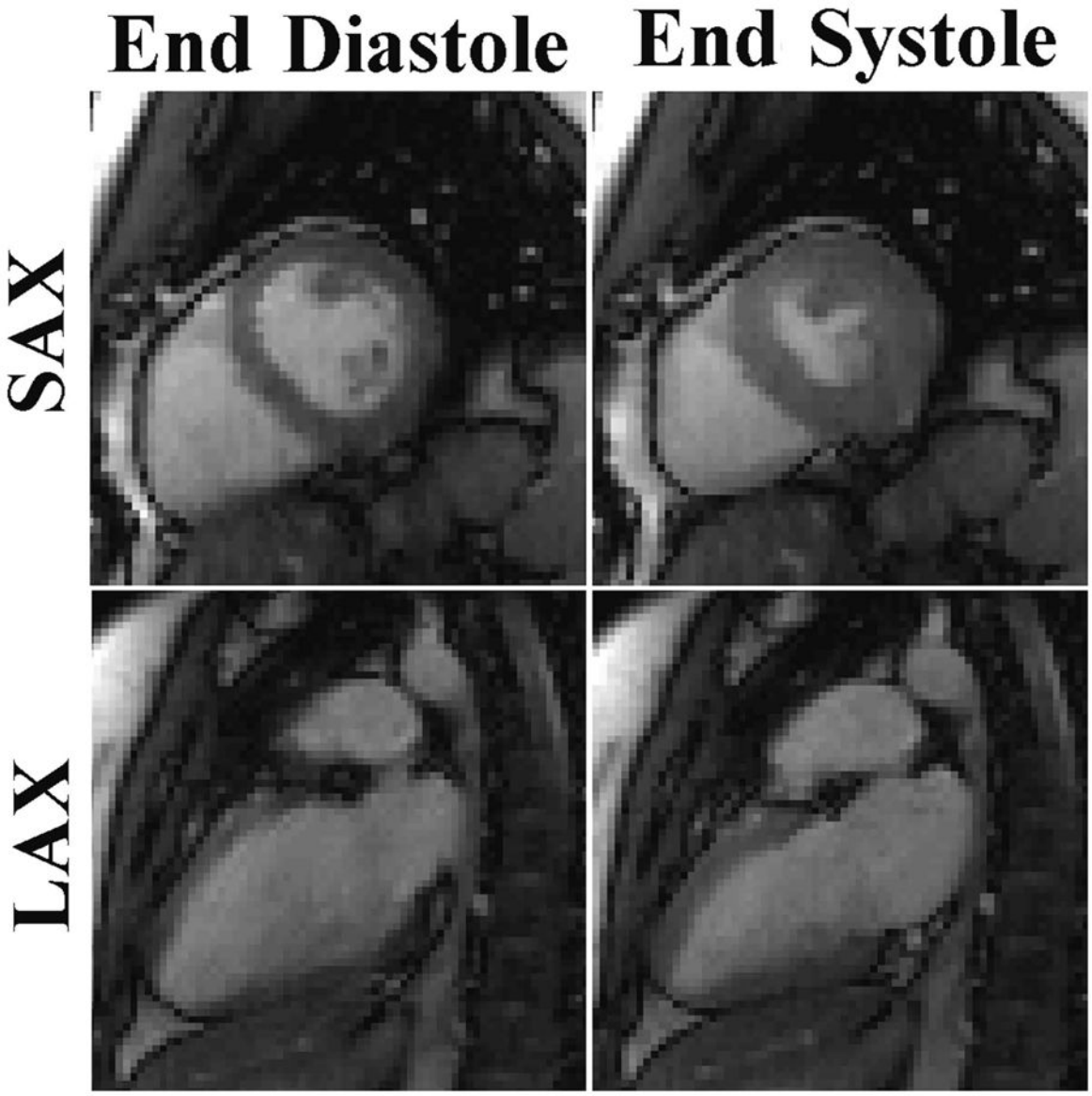

Figure 10.
Representative end-diastolic and end-systolic real-time cine images: (Top row) SAX view of a 26-year old (female) patient and (Bottom row) LAX view of a 36-year old (male) patient. The patient in SAX view exhibited averaged scores of 3.5, 4.5, 2, and 1.75 for image quality, temporal fidelity, artifact and noise level, respectively. The patient in LAX view exhibited averaged scores of 3.5, 3.75, 1.75, and 1.75 for image quality, temporal fidelity, artifact and noise level, respectively.

Table 1

Mean scores of image quality, temporal fidelity of wall motion, artifact, and noise, produced by breath-hold cine MRI and real-time cine MRI. All scores were significantly different ($p < 0.05$). For real-time cine MRI, image quality and temporal fidelity scores were above 3.0 (adequate), and artifact and noise scores were below 3.0 (moderate). In particular, averaged temporal fidelity score was above 4.0 (good). Note that temporal fidelity of myocardial wall motion is particularly important to assess regional wall motion abnormalities in the context of coronary artery disease.

Sequences	Image Quality	Temporal fidelity of wall motion	Artifact	Noise
Breath-Hold	4.6 ± 0.5	4.7 ± 0.4	1.4 ± 0.6	1.1 ± 0.2
Real-Time	3.5 ± 0.5	4.5 ± 0.4	2.3 ± 0.5	2.1 ± 0.4

Table 2

Bland-Altman and CV analyses of 4 global function measurements between real-time and breath-hold cine MRI pulse sequences.

Measurement	Mean	Mean Difference	Upper 95% Limit	Lower 95% Limit	CV (%)
EDV	143 ml	−15.2 ml	−2.8 ml	−27.6 ml	6.22
ESV	55.7 ml	2.1 ml	8.9 ml	−4.7 ml	4.42
SV	87.3 ml	−17.3 ml	−3.3 ml	−31.3 ml	8.79
EF	0.61	−5.7 %	−0.1 %	−11.3 %	4.68

Table 3

ICC analysis of inter-observer variability of EDV, ESV, SV and EF within each pulse sequence type. BH: breath-hold; RT: real-time. ICC scale: 0–0.2 indicates *poor* agreement; 0.3–0.4 indicates *fair* agreement; 0.5–0.6 indicates moderate agreement; 0.7–0.8 indicates *strong* agreement; and >0.8 indicates *almost perfect* agreement.

Measurement	ICC (BH)	ICC (RT)
EDV	0.88	0.78
ESV	0.76	0.77
SV	0.76	0.64
EF	0.64	0.64